The Planetary Science Journal, 5:236 (13pp), 2024 October https://doi.org/10.3847/PSJ/ad7a01

Macroscale Roughness Reveals the Complex History of Asteroids Didymos and Dimorphos

Jean-Baptiste Vincent[1], Erik Asphaug[2], Olivier Barnouin[3], Joel Beccarelli[4], Paula G. Benavidez[5], Adriano Campo-Bagatin[5], Nancy L. Chabot[3], Carolyn M. Ernst[3], Pedro H. Hasselmann[6], Masatoshi Hirabayashi[7], Simone Ieva[6], Özgür Karatekin[8], Tomáš Kašpárek[9], Tomáš Kohout[10,11], Zhong-Yi Lin[12], Alice Lucchetti[4], Patrick Michel[13,14], Naomi Murdoch[15], Maurizio Pajola[4], Laura M. Parro[5], Sabina D. Raducan[16], Jessica Sunshine[17], Gonzalo Tancredi[18], Josep M. Trigo-Rodriguez[19], and Angelo Zinzi[20]

[1] DLR Institute of Planetary Research, Berlin, Germany; jean-baptiste.vincent@dlr.de
[2] Lunar and Planetary Laboratory, University of Arizona, Tucson, AZ 85721, USA
[3] Johns Hopkins University Applied Physics Laboratory, Laurel, MD 20723, USA
[4] INAF-OAPD Astronomical Observatory of Padova, Italy
[5] IUFACyT-DFISTS, Universidad de Alicante, Spain
[6] INAF-OAR, Rome, Italy
[7] Daniel Guggenheim School of Aerospace Engineering, Georgia Institute of Technology, Atlanta, GA 30332, USA
[8] Royal Observatory of Belgium, Brussels, Belgium
[9] Brno University of Technology, Czech Republic
[10] Department of Geosciences and Geography, University of Helsinki, Finland
[11] Institute of Geology of the Czech Academy of Sciences, Czech Republic
[12] Institute of Astronomy, National Central University, No. 300, Zhongda Road, Zhongli Dist., Taoyuan City 32001, Taiwan
[13] Université Côte d'Azur, Observatoire de la Côte d'Azur, CNRS, Laboratoire Lagrange, Nice, France
[14] The University of Tokyo, Department of Systems Innovation, School of Engineering, Tokyo, Japan
[15] Institut Supérieur de l'Aéronautique et de l'Espace (ISAE-SUPAERO), Université de Toulouse, Toulouse, France
[16] University of Bern, Switzerland
[17] Department of Astronomy and Department of Geology, University of Maryland, College Park, MD 20742, USA
[18] Facultad de Ciencias de la Universidad de la República, Uruguay
[19] Institute of Space Sciences (CSIC-IEEC), Campus UAB, c/Can Magrans s/n, Cerdanyola del vallès, Barcelona, Catalonia, Spain
[20] ASI-Space Science Data Center, Rome, Italy
Received 2024 May 29; revised 2024 September 8; accepted 2024 September 10; published 2024 October 24

Abstract

Morphological mapping is a fundamental step in studying the processes that shaped an asteroid surface. However, it is challenging and often requires multiple independent assessments by trained experts. Here we present fast methods to detect and characterize meaningful terrains from the topographic roughness: entropy of information, and local mean surface orientation. We apply our techniques to Didymos and Dimorphos, the target asteroids of NASA's Double Asteroid Redirection Test mission—the first attempt to deflect an asteroid. Our methods reliably identify morphological units at multiple scales. The comparative study reveals various terrain types, signatures of processes that transformed Didymos and Dimorphos. Didymos shows the most heterogeneity and morphology that indicate recent resurfacing events. Dimorphos is comparatively rougher than Didymos, which may result from the formation process of the binary pair and past interaction between the two bodies. Our methods can be readily applied to other bodies and data sets.

Unified Astronomy Thesaurus concepts: Asteroids (72)

1. Introduction

NASA's Double Asteroid Redirection Test (DART) is the first planetary defense mission to attempt the deflection of an asteroid orbit. Its target was Dimorphos, a 151 ± 5 m diameter S-type asteroid, the secondary component of the 65803 Didymos system (primary's diameter: 761 ± 26 m; R. T. Daly et al. 2023). The impact successfully occurred on 2022 September 26 at 23:14:24 UTC (R. T. Daly et al. 2023) and changed the orbital period of Dimorphos around Didymos by -33 ± 1 minutes (C. A. Thomas et al. 2023). Shortly before the impact, DART acquired and transmitted high-resolution images of both asteroids. The data revealed complex surfaces with several types of terrains and morphological features like craters and boulders (O. S. Barnouin et al. 2023; R. T. Daly et al. 2023), similar to those previously observed on other asteroids (e.g., Itokawa, A. Fujiwara et al. 2006; Bennu, O. Barnouin et al. 2019; Ryugu, S. Watanabe et al. 2019).

The first step in understanding the evolutionary processes that shaped the surfaces of Didymos and Dimorphos consists of mapping the terrains and identifying the different units comprising the overall morphology. This approach is particularly useful for analyzing this binary system, as these asteroids will be revisited by ESA's Hera mission in 2027 (P. Michel et al. 2022). The morphological mapping and all information retrieved by DART before and after the impact therefore establish a reference for Hera to identify changes that may have been induced by DART in 2022, or ongoing, on both asteroids.

Establishing a morphological map is, however, challenging, as the data are limited by the resolution of imaging instruments and the viewing and illumination conditions at the time of observation. The number of images is also limited owing to the high-speed nature of the encounter, and only a handful of

observations are suited for morphological analysis. The production of a morphological or geomorphological map basically consists in recognition of visual attributes (e.g., brightness, shape) and definition of units by grouping, division, induction, or deduction. This type of map differs from geologic mapping, where the emphasis is on the timing between unit formation, the processes leading to units, and the reconstruction of the history of a terrain (D. J. Varnes 1976). While this approach has been successful for previous asteroids (e.g., 25143 Itokawa, A. Fujiwara et al. 2006; 21 Lutetia, N. Thomas et al. 2012; 162173 Ryugu, S. Sugita et al. 2019; 101955 Bennu, O. Barnouin et al. 2019), it is very time-consuming and may suffer from human biases that are not easy to quantify. To alleviate this issue, automated methods can be considered to serve as initial guidance and obtain the first assessment of the surface morphology. Examples of automated determination of morphological units on comet 67P/Churyumov–Gerasimenko can be found in J. B. Vincent et al. (2017; cliffs) and N. Thomas et al. (2018; smooth units). Both studies are based on the analysis of the tridimensional mesh of the comet's shape model.

The current work focuses on the topographic roughness (aka multiscale macroroughness, for features larger than 1 pixel). This quantity describes the variability of surface topography as a function of spatial scale. It can be expressed in different ways, like the mean slope angle of the surface with respect to its local neighborhood, or the rms height over a reference surface. A review of techniques commonly used with remote-sensing data can be found in M. K. Shepard et al. (2001).

It is well-known from previous missions that the surface of a single small body can present a large variability in roughness, typically seen as varying surface texture. Prominent examples are the localized fine-grained deposits on 433 Eros (P. C. Thomas et al. 2002) or the Muses Sea smooth terrain on 25143 Itokawa (A. Fujiwara et al. 2006); both areas contrast with their rougher surroundings. More recent studies, using high-resolution laser altimetry, are available for asteroids Eros (H. C. Susorney & O. S. Barnouin 2018) and Bennu (M. G. Daly et al. 2020) and were used to identify regions of different evolutionary states (coupled with crater counting) or assess the thickness of the mobile regolith layer.

As the roughness is inherently a measure of small-scale amplitude variations in the terrain, its estimate depends on the resolution of available observations and the scale at which it is investigated. At centimeter to meter scale, the roughness might reveal grain-size-sorting processes that mobilize the regolith across the surface (e.g., E. R. Jawin et al. 2022). At larger measuring scales, it can help to identify craters, boulders, and lineaments, or find the boundaries between ponded deposits of fine material and areas of coarser regolith. In turn, those identifications can be associated with gravitational, albedo, compositional maps, to build a full understanding of the surface.

We note that at pixel scale and below the surface roughness is usually retrieved with dedicated photometric modeling of the surface brightness per pixel, through advanced models such as B. Hapke (1984). See D. Marshall et al. (2018) for roughness studies of comet 67P/Churyumov–Gerasimenko at microwave and infrared wavelengths, or P. H. Hasselmann et al. (2021) for the optical roughness of asteroid Bennu.

Beyond small bodies, roughness and its connection to morphology have often been studied from topographic measurements of larger bodies, e.g., the Moon (M. A. Kreslavsky et al. 2013; R. M. Marshal et al. 2023), Mercury (H. C. M. Susorney et al. 2017), and Mars (J. B. Garvin et al. 2000), and show a clear correlation with regolith formation and modification, as well as bedrock geology. Roughness is also an important factor to be considered because it affects the balance of radiation and the thermal inertia. The amount and size distribution of the regolith affects the roughness. For example, asteroids smaller than 100 km are often covered by coarse regolith grains that decrease the roughness and thermal inertia (J. Hanuš et al. 2018). The situation for binary asteroids could be different as a consequence of the gravitational interactions among the bodies.

In this work, we present innovative approaches that allow for a fast determination of the surface roughness on airless bodies. Our study focuses on the topographic roughness, in order to identify features that span multiple pixels in the data. We show how techniques derived from information theory can be used to quantify the topographic roughness of asteroid surfaces at multiple spatial scales, and we automate the mapping of significant units. We apply our methods to a subset of images of asteroids Didymos and Dimorphos, acquired by DART. We provide a first description of the spatial distribution of roughness on each object and derive information about the surface evolution of the two bodies.

Our techniques are not constrained to the objects described in this paper and can be readily applied to any other application that needs to assess the roughness of a terrain. We are already implementing these techniques in the data analysis pipelines for ESA's Hera mission, which will revisit Didymos and Dimorphos. Our methods may also be considered for autonomous navigation around asteroids or obstacle avoidance during lunar landings.

2. Methods

We provide here more details on how the roughness measurement techniques work and how they are implemented. Two methods are presented: "roughness from texture" (RFT) and "roughness from shape" (RFS).

2.1. RFT: Roughness from Texture

The RFT method we developed is inspired by techniques used in information theory and defined in C. E. Shannon (1948). We measure a parameter known as the entropy of information (EOI), which can be described as the number of bits needed to encode the variability of the signal. Mathematically, it is the log-base-2 of the number of possible outcomes for a message:

$$H(X) = -\sum_{x\in\chi} p(x)\log_2 p(x). \quad (1)$$

For a variable X in the domain χ, we sum over the variable's possible outcomes x and their probability $p(x)$ of occurrence within the signal.

When applied to imaging data, we measure this parameter in a sliding window of $n \times n$ unordered pixels, across the image. This means that all pixels within the measurement window are considered equally. In this context, x is given by the encoding of the images (8-bit gray scale, i.e., pixel values are in the range 0–255), and $p(x)$ is simply the number of occurrences of a value x divided by the total number of pixels in the sliding window. Regions that present a high variability in pixel value

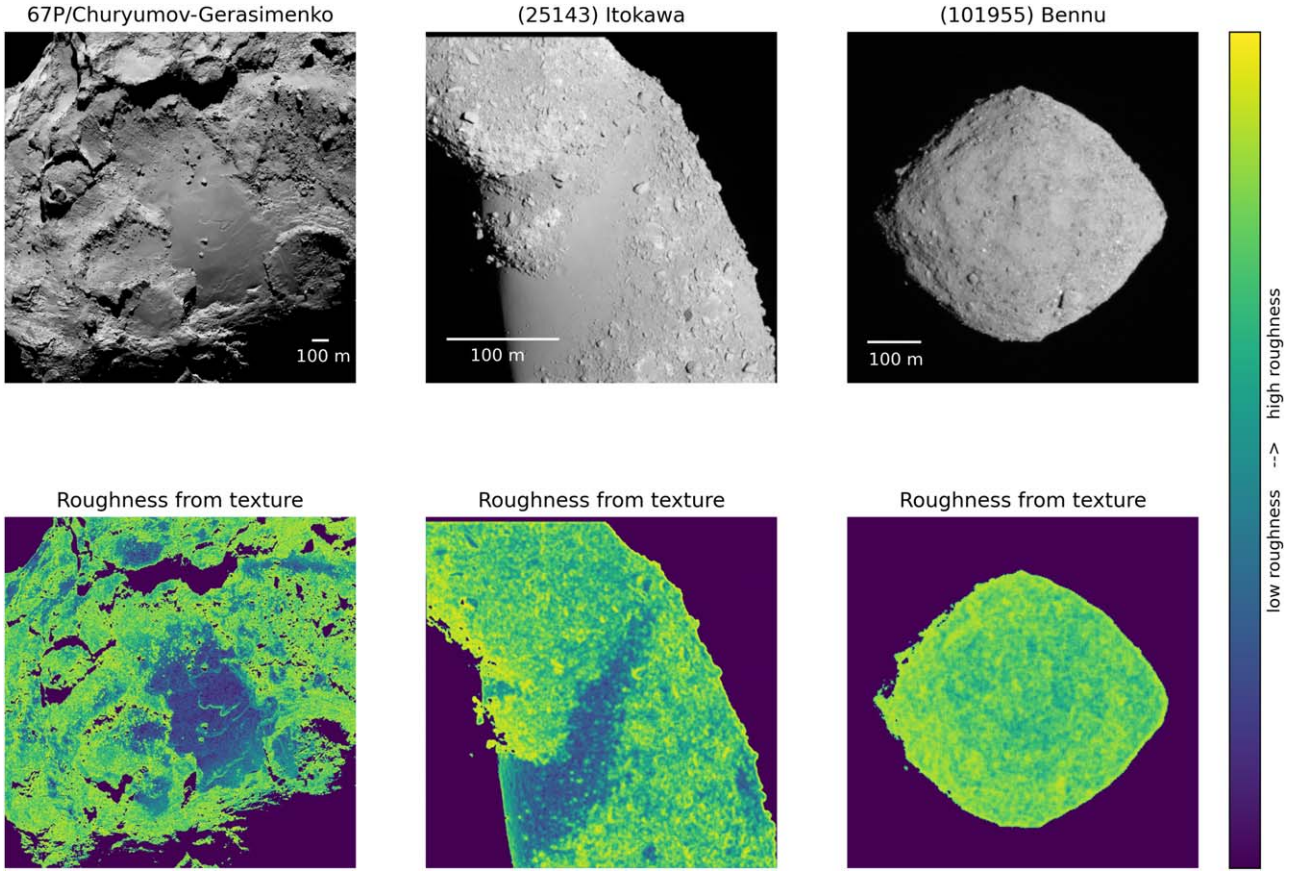

Figure 1. Top row: calibrated images of small bodies acquired by ESA's Rosetta, JAXA's Hayabusa, and NASA's OSIRIS-REx missions, from left to right. Gray scale indicates the reflectance of the surface. Bottom row: EOI measured on the same images. The low and high values of entropy match the distribution of rough and smooth terrains on all objects. All images use the same color scale. Qualitatively, 67P and Itokawa display different types of terrains, while Bennu's surface is more uniform. All data are publicly available; see Appendix A.

will be characterized by a high entropy, while regions with uniform pixel values will have a low entropy.

The choice of a logarithm base depends on the application. Here we chose to use $\log_2$, which gives an EOI expressed in bits; $\log_2$ also has the advantage of being often implemented directly on the hardware (i.e., instruction FYL2X in Intel x86-assembly) and therefore extremely fast to calculate. This is particularly relevant for the use of this technique in embedded software, e.g., for autonomous navigation on board a spacecraft where computing resources are limited.

Photometric models typically consider incident, emission, and phase angles, as well as surface albedo and several correcting factors. Typically for asteroids, brightness variation across the surface is mostly a function of the local topography (i.e., incidence and emission). We must, however, be wary of observations at low phase angles (typically i, $e < 10°$), where additional effects such as shadow hiding and coherent back-scattering play a major role and nontopographic parameters like composition and grain size must be accounted for. In a similar fashion, observations at high incidence angle can also be problematic, as the long shadows will obscure part of the terrain and also create artificial high-entropy boundaries, where the border between shadowed and illuminated terrain is seen as a large jump in pixel values. This is, however, a well-known problem with the interpretation of imaging data for asteroids, and we preempt it by selecting data and observing conditions that avoid extreme values of i and e, as well as masking potentially problematic areas in the images (shadows). With these precautions, our technique relies on the same principles behind digital terrain model reconstruction methods like photoclinometry (aka "shape from shading"), routinely used by space missions to reconstruct the local terrain.

Therefore, we use the EOI (pixel value variability) as a proxy for a measure of the variability of incidence and emission, which is controlled by the local slope of the terrain. This means that the measure of EOI informs us directly about the roughness of the surface, at a scale defined by the size of the neighborhood in which we calculated the entropy.

Figure 1 shows examples of entropy measurements on several asteroids and comets, as well as the clear correlation between the entropy value and the actual roughness of the surface. Note that this paper introduces the method and applies it to the specific case of Didymos+Dimorphos images returned by the DART mission. A follow-up study of asteroid surface roughness that applies our methods to all objects imaged so far is ongoing and will provide a quantitative comparison with previous works. First results are presented in C. Herrmann & J.-B. Vincent (2024).

A strong advantage of this method is that it does not require prior knowledge of the photometric response of the surface. More specifically, the results are independent of the viewing angles (incidence, emission, phase) as long as one avoids extreme situations: e.g., at phases below 20°, the brightness variations must account for albedo and material properties. In most images, however, the phase can be ignored, as the entropy measure depends on the number of state transitions (how often

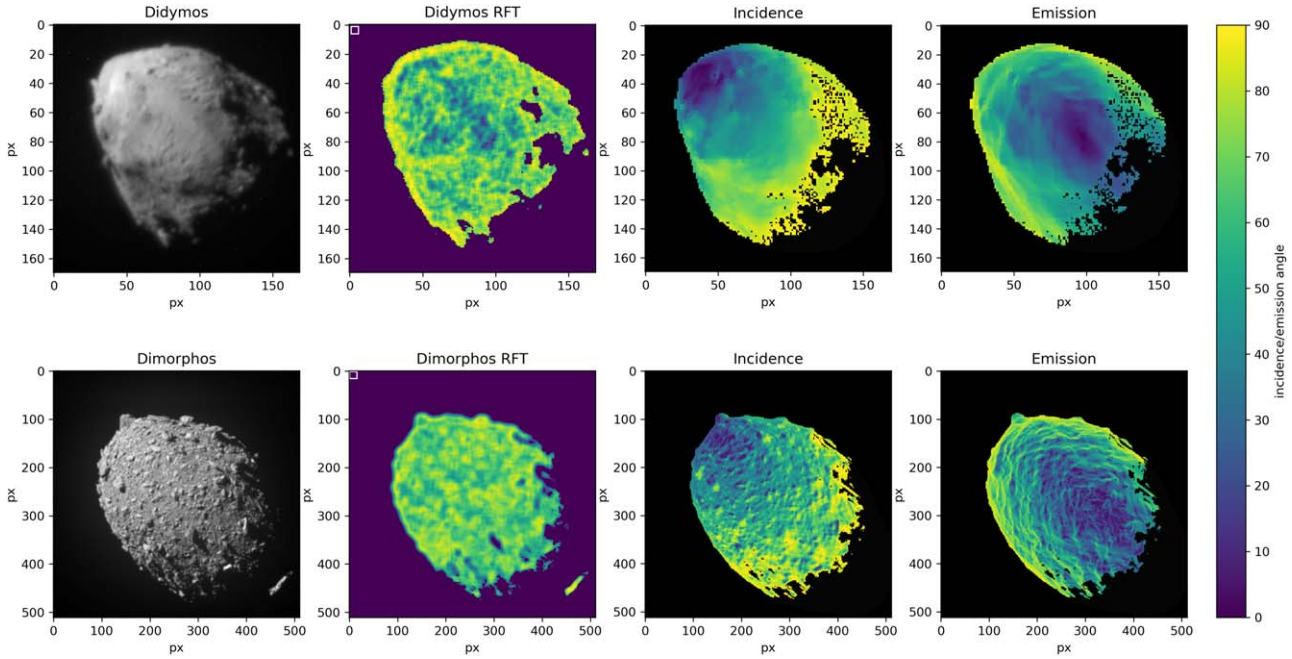

Figure 2. Comparison between the RFT and the illumination angles (incidence and emission) on Didymos and Dimorphos at the time of image acquisition. There is no apparent correlation between these quantities, which suggests that the measurement is robust against a wide range of illuminations. Top row: resolution is 5 m pixel^{-1}; bottom row: resolution is 0.35 m pixel^{-1}.

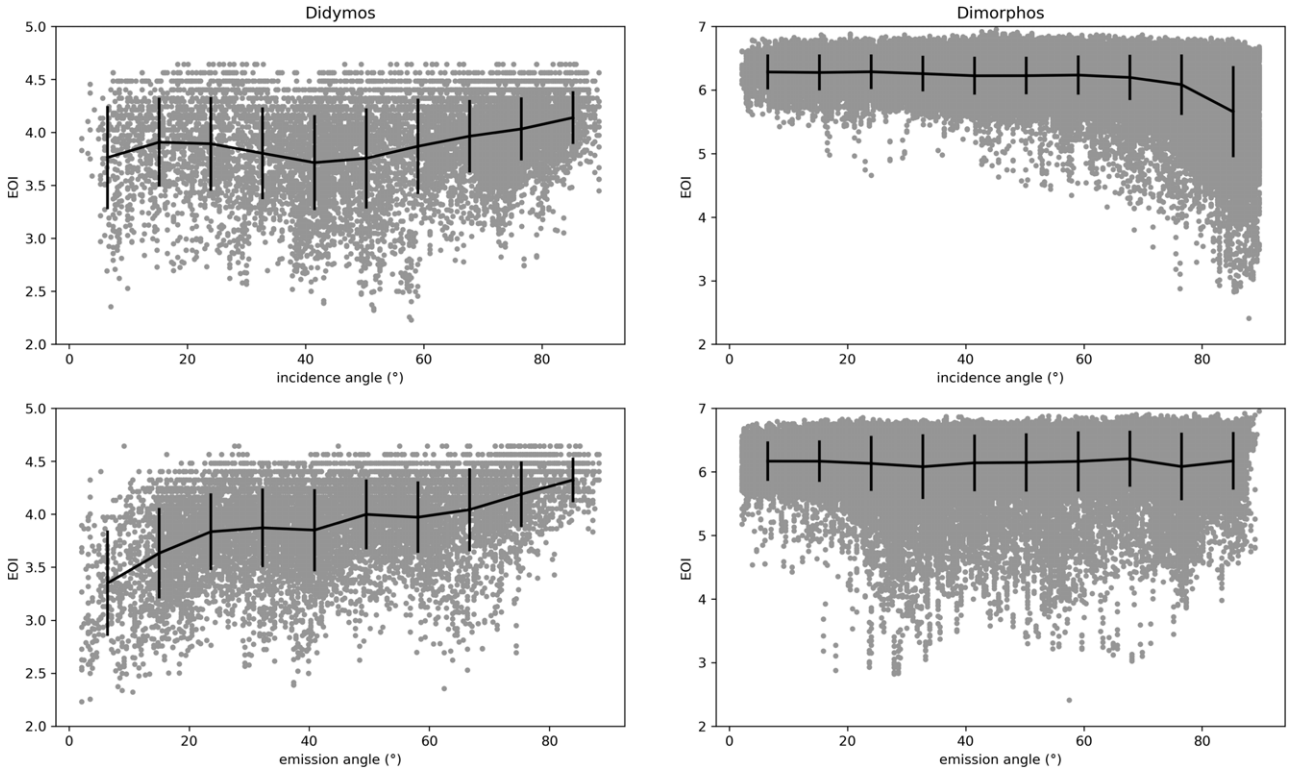

Figure 3. EOI vs. incidence and emission angles for both asteroids; mean and standard deviations are calculated in bins of 10°. The EOI does not correlate with incidence and emission, except for extreme angles (i, $e < 20°$ and i, $e > 80°$) where photometric effects and long shadows start to become significant.

do pixel values change) rather than the states themselves (absolute difference between pixel values). This means that low-contrast and high-contrast images of the same area have the same entropy, as long as the topography can be detected (again, ignoring opposition and shadows). Figures 2 and 3 show how incidence and emission angles can essentially be ignored when measuring the roughness with our method on Didymos and Dimorphos, as long as we avoid the more extreme angles.

Besides measuring roughness, our technique can also be used to identify surface changes. By measuring the entropy of the same region at two different epochs, one can determine

precisely which areas have seen their texture modified. The technique has been applied successfully to track changes on comet 67P (boulder fields covered/exposed by dust deposition/removal, dune displacement, formation of circular depressions, etc.); see J.-B. Vincent et al. (2021).

We note that the technique is easy to implement and readily available in most image processing software/libraries. This paper, for instance, used the function available in the open-source Python library *scikit-image*.[21]

2.2. RFS: Roughness from Shape

The RFS method operates on a totally different set of data. Rather than considering pixel values in images, we measure the variability of the topography on a reconstructed three-dimensional model of the object of interest. A shape model is a collection of points in 3D space, linked together in a closed mesh of polygons (typically triangles). For each facet, one can measure its orientation in the body-fixed frame and compare it to other facets in a given neighborhood. There are several ways to achieve this, which can be found in the literature and have been applied to solar system bodies, or everyday objects (e.g., Gowman et al. 2023). The most commonly used technique consists in measuring the rms distance between facet centers and a reference baseline surface (H. C. M. Susorney et al. 2019). Other authors (M. Egorov et al. 2017) have also considered comparing the orientation of a facet in a high-resolution model with the same location on a lower-resolution shape within the same reference frame.

In this paper, we use a slightly different approach that aims to minimize the number of free parameters. Like M. Egorov et al. (2017), we are interested in the local variation of facet orientation. However, we use the highest-resolution shape model of our target and do not introduce low-resolution models, to avoid uncertainties that arise from the decimation process. Instead, for each facet, we measure the angle between its normal vector and those of its neighboring facets. The mean value of this angle is our roughness parameter. To control the scale of the measurement, one can adjust the number of neighbors to be considered. Those can be limited to the immediate three neighboring triangles, or include all facets within a certain distance of the point of interest. "Distance" can be measured in different ways: shortest path on the surface, latitude/longitude difference, number of neighbors from the starting point, etc.

This technique has the advantage of not requiring any data other than the original shape model. It is purely geometrical, making no assumptions about the internal state of the target (gravity is irrelevant). Because our measurement only depends on the local facet orientation within a given neighborhood, the results can be directly compared to what is obtained with the RFT method, which, at the scales considered here (tens of centimeters and larger), also depends primarily on the terrain geometry, as discussed earlier.

Of course, we must mention the caveat that our technique is applied to a secondary product (shape model). Hence, the interpretation of our results must account for any uncertainty pertaining to the method used to create that specific model.

[21] https://scikit-image.org. The code implementing the entropy function for this library can be found at https://github.com/scikit-image/scikit-image/blob/main/skimage/filters/rank/generic.py.

The computation can be quite demanding, as the file formats used for 3D models of asteroids (e.g., OBJ) do not store information about facet neighbors. Determining whether two facets are neighbors requires checking whether they share an edge, i.e., they have two common vertices. A naive way to do this is to load all facets and, for each of them, loop once through the whole list and identify neighbors. One can speed this up by stopping the secondary loop as soon as three neighbors are found and double-allocating neighbors (if B is a neighbor of A, then A is a neighbor of B). Still, this approach is very time-consuming for models that have millions of facets.

For this work, we have implemented a faster approach to find all neighbors as we load the shape, requiring only one pass through all facets. The pseudo-code for the method is given hereafter in Algorithm 1.

Algorithm 1. Build list of neighbors for each facet.

Notes on syntax: $A[i]$ means *value at index* i in array A. $x \leftarrow y$ means *variable* x gets the value y.
Require: list of N facets, defined by their vertices: $Facet[f] = [i, j, k]$ where f is a facet index and i, j, k are indices of elements in a list of vertices
  $Edge \leftarrow$ empty array
  For facet index f in range $[0, N]$ **do**
    $v_0 \leftarrow Facet[f][0]$
    $v_1 \leftarrow Facet[f][1]$
    $v_2 \leftarrow Facet[f][2]$
    $Edge[3 \times f + 0] = [min(v0, v1), max(v0, v1), f]$
    $Edge[3 \times f + 1] = [min(v1, v2), max(v1, v2), f]$
    $Edge[3 \times f + 2] = [min(v2, v0), max(v2, v0), f]$
  end for
  Sort $Edge$ list by first column
  For each value of first column, sort $Edge$ list by second column
  $e \leftarrow 0$
  While $e < length(edge)$ **do**
    $f_a \leftarrow Edge[e][2]$
    $f_b \leftarrow Edge[e + 1][2]$
    Append f_b to $Facet[f_a]$.
    Append f_a to $Facet[f_b]$.
    $i \leftarrow e + 2$
end while

The algorithm guarantees that all neighbors are found uniquely, and reading the Edge list two rows at a time gives a list of pairs of neighbors.

After the neighbors of each facet have been determined, it is trivial to calculate the roughness as a mean orientation angle using simple geometry. For a facet defined by three vertices $[v_0, v_1, v_2]$, the normal vector is given by the cross product between the vectors positioning any pair of clockwise consecutive vertices in the body-fixed frame (e.g., $\boldsymbol{v}_0 \times \boldsymbol{v}_1$). The angle θ between two facets is derived from the dot product between two normal vectors:

$$\cos(\theta) = \frac{\boldsymbol{n}_1 . \boldsymbol{n}_2}{||\boldsymbol{n}_1|| \times ||\boldsymbol{n}_2||}.$$

We implemented this approach in the data analysis tool *shapeViewer*[22] (J. B. Vincent 2018). Our code (C language) can process a shape model with 1 million facets in a couple of seconds on a standard laptop (the slowest machine tested has

[22] Scientific software freely available at https://www.comet-toolbox.com.

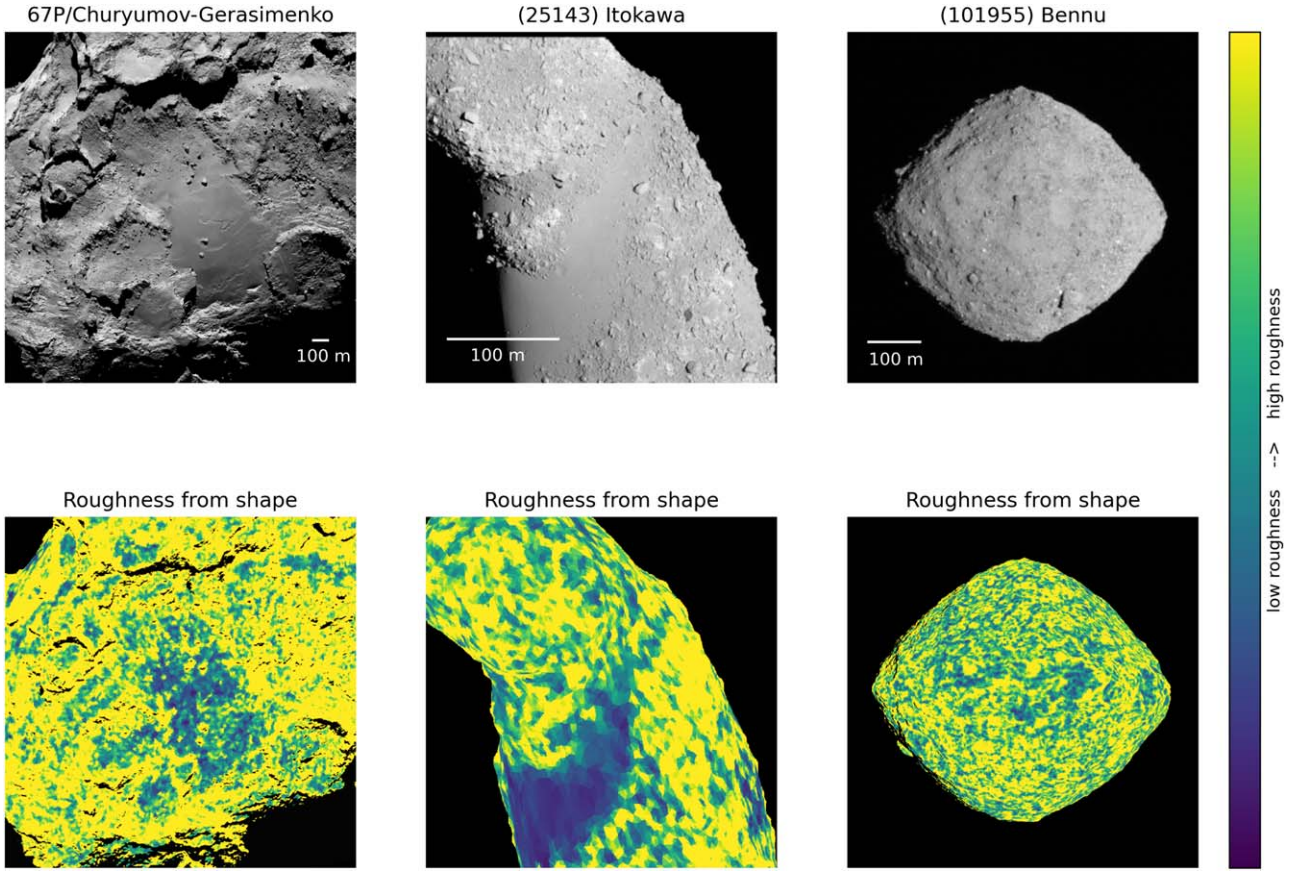

Figure 4. RFS method applied to the reconstructed tridimensional models of comet 67P/Churyumov–Gerasimenko and asteroid (25143) Itokawa. Models taken from public archives; processing and rendering done with *shapeViewer* (J. B. Vincent 2018). We use the same reference images as in Figure 1. The smooth/rough terrains visually identified in the images of 67P and Itokawa can also be found in the RFS measurements, albeit within the limitations of the shape model resolution. The spatial distribution of RFS on Bennu appears less localized than on the other bodies, with no obvious units. Note that this figure only shows a qualitative example of the method. A thorough comparison of RFS measurements across asteroids, as well as comparison with previous methods, is given in C. Herrmann & J.-B. Vincent (2024).

2 GHz CPU and 4 GB RAM). While this is sufficient for our needs, we note that the algorithm could be sped up by parallelizing the construction of the edge list and selecting a different sorting method (we used quicksort).

Figure 4 shows examples of RFS measurements on several asteroids and comets; smooth regions are clearly identified and match those found in Figure 1 with the RFT method.

3. Results

Because the DART spacecraft flew by Didymos and impacted Dimorphos at 6.14 km s^{-1} (R. T. Daly et al. 2023) on an almost straight-on trajectory (only 16.°7 from vertical), all images obtained by the Didymos Reconnaissance and Asteroid Camera for OpNav (DRACO; Z. J. Fletcher et al. 2022) present essentially the same viewing geometry and illumination conditions, with only a change in resolution. In this work, we focus on two specific observations: the highest-resolution image of the full sunlit Didymos system (which also contains the highest-resolution image of the full sunlit primary), and the highest-resolution image of the full sunlit secondary, Dimorphos. Both observations are shown in Figure 5. We use the calibrated data publicly available in NASA's Planetary Data System archive (C. Ernst et al. 2023) with no additional processing.

We first characterize the surface roughness of both asteroids by measuring the distribution of EOI in these two images, as introduced in Section 2.1. As a reminder, the EOI describes the average amount of information contained in a signal (C. E. Shannon 1948). A rapidly changing signal (either spatially or in time) is considered rich in information (high entropy), while a monotonous signal with little variability is poor in information (low entropy). When applied to imaging data, the signal considered is the distribution of pixel values across the image. The entropy is measured at different scales by considering subregions of different sizes in the images, like usually done with spatial filtering (R. Gonzalez & E. Woods 2008).

This technique has been used for many decades to classify signals or retrieve information in noisy backgrounds and is readily available in most signal processing or digital image processing software packages. Despite its numerous benefits, we found that the technique has seldom been used in planetary science. To the best of our knowledge, the method has previously only been applied to characterize the roughness of topographic maps derived from laser altimetry (e.g., B. Li et al. 2015). Our work is the first application of the method to study primary data products such as camera images.

A strong advantage of the method is that it is mostly unaffected by the photometric properties of the surface, as long as we avoid areas with extreme observing and illumination angles, for instance, the opposition effect at low phase angle, or long shadows at high incidence angles. Under typical observing conditions encountered by space missions (i.e., $20° <$ phase angle $< 80°$) and for uniform albedo surfaces (most asteroids),

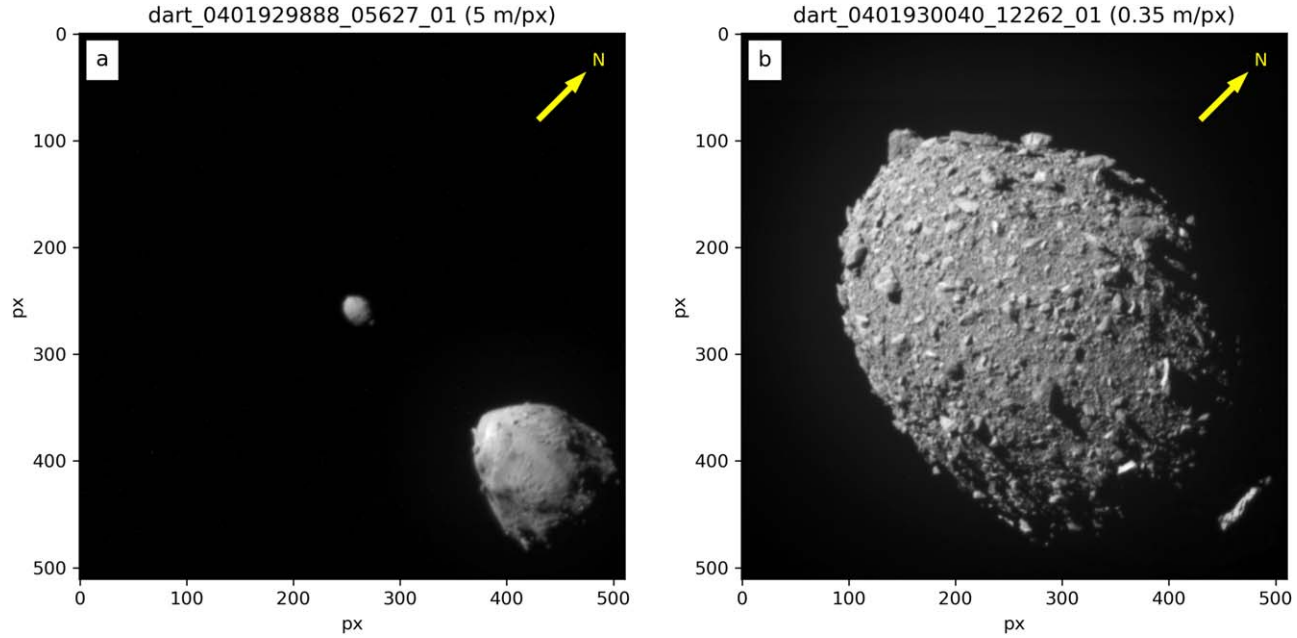

Figure 5. DRACO images of Didymos and Dimorphos acquired respectively 2 m 43 s (panel (a)) and 11 s (panel (b)) before impact. The yellow arrow indicates the direction of the north pole of both asteroids (Didymos's positive spin axis).

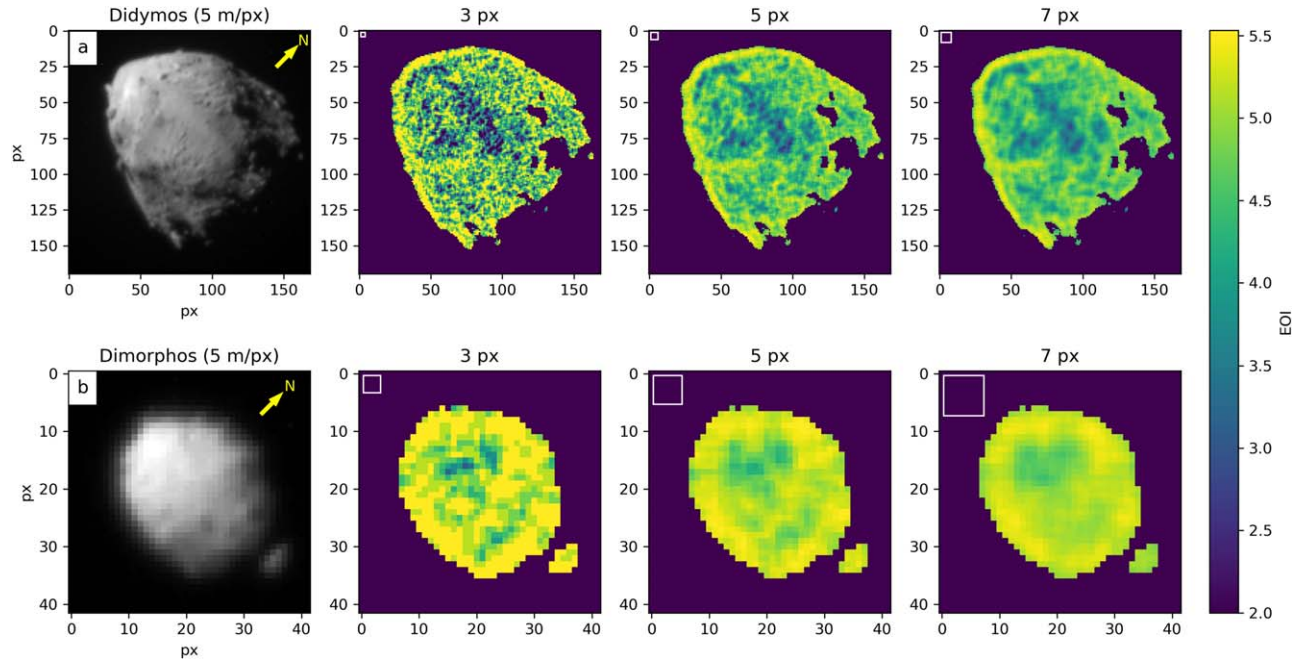

Figure 6. EOI measured on (a) Didymos and (b) Dimorphos at multiple scales. Image resolution is 5 m pixel^{-1}; the measurement scale is given in pixels and also represented visually by a white square in the upper left corner of each panel.

the entropy is directly a function of the surface topography at the scale of interest.

Note that because the method is based on the analysis of pixel values in the images, we sometimes refer to it as RFT, in opposition to alternative methods that are typically based on a shape model (referred to as RFS).

3.1. General Observations and Comparative Analysis at 5 m pixel^{-1}

Figure 6 displays a comparative view of the EOI on both asteroids at a resolution of 5 m pixel^{-1}. In these images, we measured the EOI at different spatial scales, represented by sliding boxes of $n \times n$ pixels across the images. Here we used scales of 3, 5, and 7 pixels, which correspond to distances of 15, 25, and 35 m on the surface. All observing conditions (resolution, illumination, viewing angle, etc.) being equal, this allows a direct comparison of the EOI measurement between the two bodies. Of course, at this resolution, Dimorphos is only 20 pixels wide, while Didymos is five times larger. Still, as long as the entropy measurement scale is smaller than the asteroid, we obtain a description of the roughness across the surface that consistently matches the qualitative identification by trained experts.

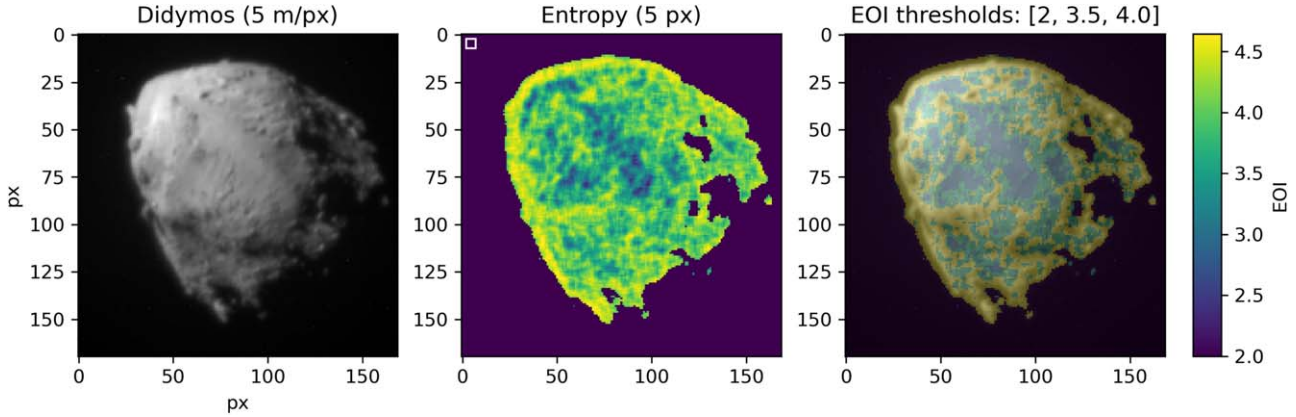

Figure 7. EOI measured on Didymos at 5 m pixel^{-1}. The thresholds in EOI values have been chosen to enhance the location of smooth, intermediate, and rough terrains on the asteroid.

There are a couple of artifacts to be aware of when analyzing results such as shown in Figures 6, 7, and 9. First, we have masked all shadowed areas and space beyond the asteroid. This is to avoid that low-level noise interpreted as signal. It is possible for very sensitive cameras to actually "see in the dark" when imaging shadowed terrains faintly illuminated by scattered light from nearby lit surfaces. That is, however, not the case for this data set. Second, the border between a shadowed region and a lit region shows up as a high-entropy edge in our analysis, because pixel values vary by a large amount over a short distance. This leads to an increase of entropy close to the darkest shadows, as well as around the asteroid limb, and must be taken into account when interpreting the results.

As explained in Section 1, one of the goals of our method is to assist in the definition and characterization of morphological units. This is achieved by defining thresholds and sorting the surface entropy values in a limited number of bins that correspond to specific morphology. As the entropy values are expressed in bits and do not have a direct physical meaning, we first consider the typical entropy values of areas that would be unambiguously characterized as smooth/rough by trained morphology experts in the data being investigated. We then segment the images according to these thresholds. For bodies whose surfaces show starker differences in roughness level, this process could eventually be automated by identifying peaks in the histogram of entropy values.

Our results are shown in Figures 7 and 9 and discussed hereafter:

1. Both asteroids display significant variations in EOI, unrelated to the observing conditions (no correlation between roughness values and incident, emission, or phase angles; see Section 2.2 for additional information). This is indicative of varied roughness levels at the scales considered.
2. Both asteroids show a nonrandom distribution of smooth and rough terrains. We detect patterns that persist at multiple scales and may indicate boundaries between morphological terrains, or subsurface structures (see Sections 3.2 and 3.3).
3. We confirm that smooth terrains on Didymos appear to be mostly located in the equatorial regions, while mid- and high latitudes are rougher, in agreement with the morphological analysis in O. S. Barnouin et al. (2023). On the contrary, but also in agreement with those authors, we do not detect such dichotomy on Dimorphos. We note that other authors have reported a longitudinal variation in subpixel photometric roughness (B. J. Buratti et al. 2024). These remain unexplained at the time of writing this paper, but they could be linked to dust flow features arising from Didymos and depositing on Dimorphos. These features are, however, too faint to be detected at the topographic scale investigated here.
4. The equatorial regions of Didymos are the smoothest terrains found in the system.
5. Across the scales considered, Dimorphos's surface displays, on average, the same level of roughness as the rougher terrains on Didymos.

We now look at each object in more detail and discuss the interpretation of EOI at the highest available resolution.

3.2. Didymos

Didymos shows unambiguous patterns in its distribution of topographic roughness, with its smoothest regions being located close to the equator (Figure 7). This is particularly visible in the thresholded entropy image that shows a factor two difference between the entropy level at higher latitudes and the equatorial measurements. When thresholding the EOI images, we found it useful to introduce three levels of roughness that accurately map the smooth terrains, rough terrains, and intermediate zones that would correspond to the edges of the landslides mentioned previously. Our determination of morphological units matches the geological investigation (O. S. Barnouin et al. 2023). This is illustrated in Figure 8 for a couple of morphological units.

We identify lobate smooth areas at midlatitudes that are characterized by a sharp edge at higher latitudes and a rougher edge at lower latitudes, overlaying the smooth equatorial terrain. We interpret these features as being indicative of mass wasting, with the material flow seemingly oriented from high latitudes (sharp edge where the slope broke) to low latitudes (rougher edge where a debris apron accumulated). Some ridges can be identified as well in between troughs, the combination of which could indicate formation by either incision (channels) or accumulation (debris flow), or both.

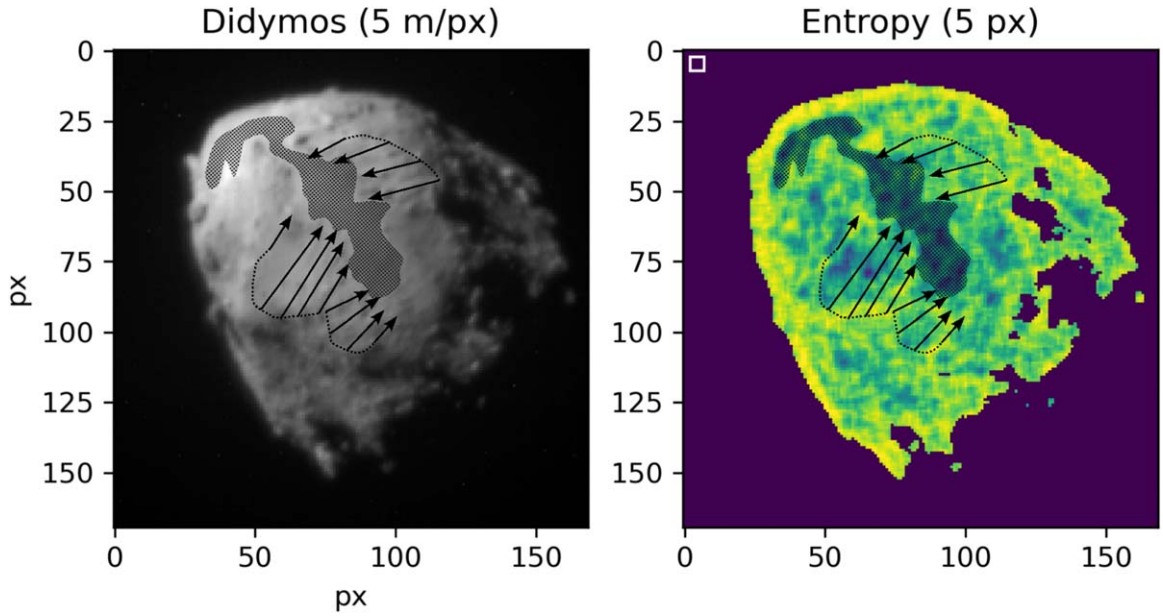

Figure 8. Example of a morphological unit identified on Didymos, overlaid on the original image and the map of EOI. The dotted area shows the contiguous smooth equatorial region. Dotted lines and arrows indicate putative mass wasting. A complete description of the geological units is available in O. S. Barnouin et al. (2023).

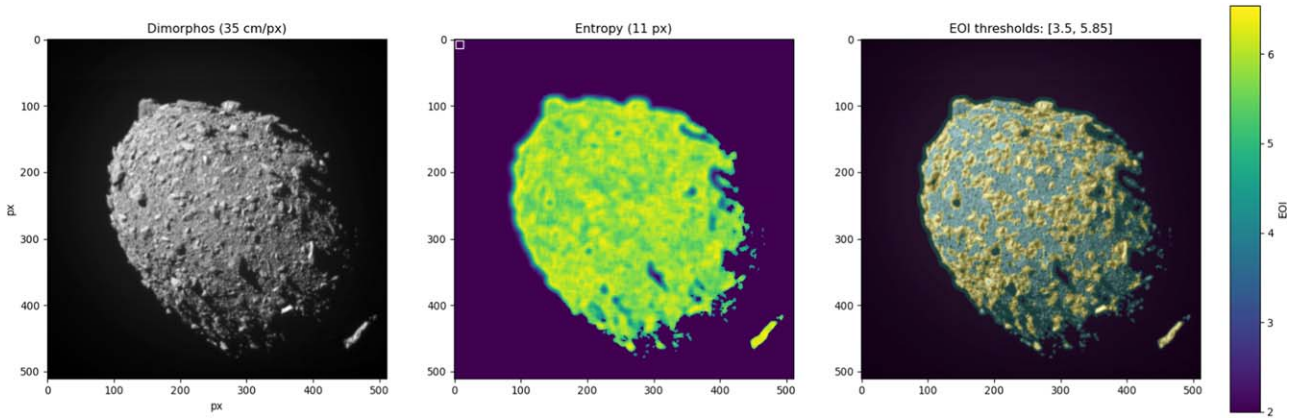

Figure 9. EOI measured on Dimorphos at 35 cm pixel^{-1}. The thresholds in EOI values have been chosen to clearly separate boulders from pebbles.

3.3. Dimorphos

By contrast with its larger companion, Dimorphos presents a much more homogeneous surface, on average rougher than Didymos's at all scales (Figures 6 and 9). We do not find any smooth region on the surface, which is dominated by high-entropy terrains. However, the EOI is not randomly distributed, and sorting the values into two bins leads to a clear separation between boulders and regolith at the chosen scale. Figure 9 shows an example of this categorization, where meter-size boulders are clearly identified by the entropy measurement. This detection is consistent with the distribution reported in M. Pajola et al. (2023), where the authors manually mapped 4734 boulders on the surface.

The efficient detection of meter-size objects is due to two supporting factors: (1) we selected an entropy window size smaller than the objects, and therefore the filter acts as an edge detector; and (2) there is an intrinsic difference in roughness between boulders and regolith substrate, at the resolution considered.

At scales smaller than boulder size, and for our observations at resolutions ranging from 0.35 to a few meters per pixel, the visible facets of boulders appear smoother (lower roughness) than the surrounding terrains. Boulders on small bodies can fall in different categories like monolith or aggregate depending on their physical and mechanical properties (i.e., porosity, strength). Different types of boulders can be found on single bodies, often suggesting a complex history (R. Jaumann et al. 2019).

In the case of aggregates, we find that the small-scale roughness on boulders and regolith is comparable, indicating that small-sized objects are very likely detached fragments from larger entities (see, e.g., K. A. Otto et al. 2020). Here the relatively lower roughness of boulder faces shows that boulders are either monolithic or aggregates made of much smaller pieces than the surrounding pebbles. The monolithic hypothesis is consistent with morphological studies (C. Q. Robin et al. 2024), which demonstrate that boulders and pebbles are very likely to originate from collisions and are themselves the fragments of larger objects. Likewise, albedo measurements (B. J. Buratti et al. 2024) indicate that objects on Dimorphos are likely to share the same composition and physical properties. Therefore, we posit that boulders on Dimorphos are more likely to be monolithic entities rather than

agglomerates of pebbles with the same size distribution as the surrounding pebbles. This hypothesis will be tested when ESA's Hera mission returns detailed spectral and mechanical measurements of the asteroid material in 2027 (P. Michel et al. 2022).

We stress that for all objects the EOI provides a reliable qualitative estimate of the distribution of smooth and rough terrain, as well as morphological features of interest within those terrains. One must, however, be cautious about quantitative comparisons, which can only be performed when all measurement parameters are kept constant. We particularly emphasize that it is critical to use objects or areas images at similar resolution, and the entropy is measured at the same spatial scale. In general, we recommend prioritizing the use of high-resolution images, even when measuring roughness at large spatial scales. The low resolution may hide topographic features.

At 5 m pixel^{-1}, we do not find any terrain on Dimorphos that would be as smooth as the equatorial regions of Didymos, possibly indicating the absence of small particles, although this cannot be proven from the low-resolution images only. Higher-resolution images of the impact site obtained in the last seconds confirm that the surface of Dimorphos does not have expansive smooth deposits where there were regolith particles that were unresolved at 5.5 cm pixel^{-1} (R. T. Daly et al. 2023).

We acknowledge that DART observed mostly the leading side of Dimorphos (with respect to its orbit around Didymos). Other regions, in particular the areas facing toward or away from Didymos, may display a different morphology or boulder distribution, possibly affected by tides induced by the primary. These terrains will be observed by the European Space Agency's Hera mission, scheduled to launch in 2024 October.

3.4. Roughness from Shape

As we measure the entropy on the calibrated images, with no further processing, one may have to consider the potential distortions induced by the asteroid shape itself: a pixel of an area with high emission angle covers, for instance, a much larger surface than a pixel at nadir. This effect must be taken into account when discussing roughness per area and can be corrected using ortho-rectified images (i.e., images projected onto a common reference frame). This is particularly important if one wants to study the evolution of roughness over time, with multiple images of the same region that may have been acquired from different viewpoints (J.-B. Vincent et al. 2021). Here we are less concerned about the effect of the shape, as we work on single images and do not compare several viewing observations. We also show in Figure 2 that, for this data set, the viewing and illumination angles of singular pixels do not affect the distribution of entropy values.

Still, in order to validate our approach, we also measured the roughness using a more traditional method of directly comparing the topography with a reference baseline, as done in other studies. However, we do approach this measurement in a new way (see Section 2.2), in which the baseline is not constrained by free parameters, but is rather directly calculated on the shape model itself. Our RFS measures the mean angle between the orientation of a facet on the shape model and its neighbors. The size of the neighborhood determines the spatial scale at which the roughness is measured.

We based our measurements on the highest-resolution shape models obtained by the DART team (Didymos: E. E. Palmer et al. 2022; Dimorphos: R. T. Daly et al. 2023), and publicly available (see Appendix A). The models have a ground sample distance (separation between vertices) of 25 cm for Dimorphos and 1.2 m for Didymos and were resampled to a resolution comparable to the smallest scale at which we measured the EOI in the images (25 m for Didymos and 3.85 m for Dimorphos), using the open-source software Meshlab[23] and its implementation of the resampling algorithm provided in M. Garland & P. S. Heckbert (1997), which preserves the original orientation of the surface.

We find that the roughness calculated on the shape model (Figure 10) matches very well what we obtained with the RFT. In particular for Dimorphos, the apparent dichotomy between boulders and regolith detected with the EOI also appears clearly with the RFS method: boulders are detected as areas with rapidly changing local angles on the digital terrain model, which translates into high-entropy regions in the images.

The match is not as good on Didymos. This is mostly due to the fact that the tridimensional shape reconstruction of this object is far more challenging because of the limited data available. Essentially, DART returned only a couple of images of Didymos at a resolution <5 m pixel^{-1}, with very little variation in viewing geometry. This limits the scale at which surface features can be reliably reconstructed. On a large scale, though, the analysis of the digital shape model confirms the presence of smoother areas in the equatorial regions and rougher terrains at higher latitudes.

Overall, we find that both methods converge qualitatively toward a similar description of the asteroid surfaces. In general, for a quantitative assessment, all roughness analysis should be performed on high-resolution 3D shape models. Obviously, that is not always possible. Reconstructing accurately the shape of an asteroid from space images usually requires weeks of effort and large computer resources. Here we have shown that a technique like the EOI provides a reliable first description of the surface and identification of major terrains and landforms of interest like boulders for a much lower cost (fraction of a second). This has implications for onboard autonomous navigation systems, for instance, which do not have the processing resources to work with 3D models.

4. Discussion

In summary, we have analyzed images returned by NASA's DART mission via novel approaches that aim to provide a fast identification of different terrain types. We use our method to derive a first characterization of the topographic roughness of asteroids Didymos and Dimorphos.

The mapping of morphological features on Didymos, and particularly areas that we interpret as indicative of mass wasting, is consistent with our understanding of the current state of Didymos. With a rotation period of 2.26 hr (S. P. Naidu et al. 2020) and an estimated mass of 5.6×10^{11} kg (O. S. Barnouin et al. 2023), the centrifugal force at the equator of Didymos is comparable in magnitude to the gravitational acceleration ($\simeq 2.2 \times 10^{-4}$ m s^{-1}). This means that the surface at low and midlatitudes may be only held together by nonzero mechanical strength and is likely to be easily mobilized, even by the smallest perturbations. Additionally, several authors (e.g., K. J. Walsh et al. 2012; Y. Zhang et al. 2021) have proposed that top-shaped asteroids spinning at a short spin period may structurally fail on their surface if there is a

[23] https://www.meshlab.net

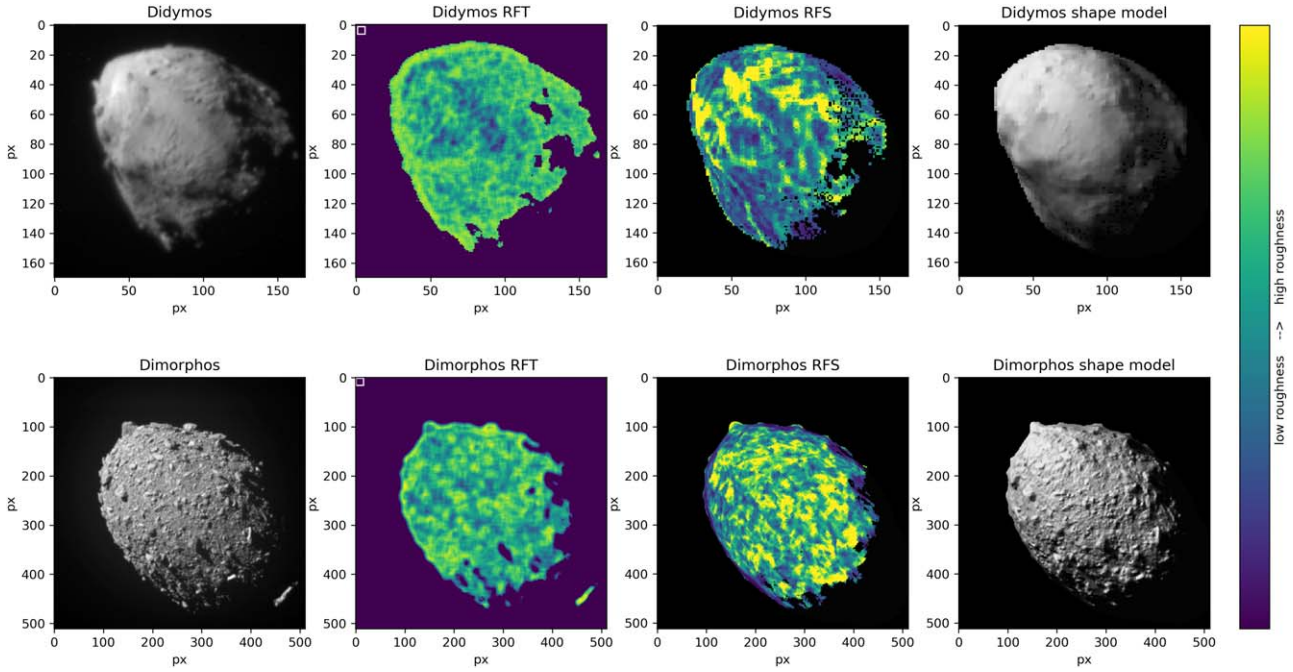

Figure 10. Comparison between RFT and RFS. Colors indicate qualitatively the distribution of smooth and rough terrains. Both methods lead to a similar description of the surfaces of Didymos and Dimorphos. Top row: resolution is 5 m pixel^{-1}; bottom row: resolution is 0.35 m pixel^{-1}. The shape models are oriented and shaded using the same geometric conditions as at the time of image acquisition.

mechanically strong interior. If there is no such strong interior, then the interior fails first, the deformation mode triggering surface failure, causing catastrophic disruption (M. Hirabayashi et al. 2022). However, recent work also shows that the spin period also changes the failure mode (M. Hirabayashi & D. J. Scheeres 2019). Surface layers may be more sensitive at a longer spin period, given almost zero cohesion; on the other hand, interiors may be more sensitive at a shorter spin period, needing higher mechanical strength (M. Hirabayashi et al. 2020). In summary, these findings suggest that while Didymos's highly oblate shape likely came from internal failure (O. S. Barnouin et al. 2023), its current surface can also be sensitive to mass wasting without internal failure, given the existence of internal mechanical strength to support the current shape.

The equatorial regions are, therefore, areas where we expect to find landslides, but also where dust might be able to stick to the surface better than boulders (cohesion of granular matter increases with decreasing particle size (L.-O. Heim et al. 1999; D. Scheeres et al. 2010; P. Sánchez & D. J. Scheeres 2014). The spatial distribution of roughness level, as shown in Figure 7, seems to indicate some form of stratification, with terrains that appear layered over others and display characteristic features of mass wasting as explained above: a sharp upper edge where the slope initially failed (scarp), a smooth flow area with few boulders that did fully reach the end of the run (channel), and a rough talus at the bottom of the slope as an accumulation of the mass-wasted material. These areas appear to be preferentially oriented from higher latitudes toward the equator, which is consistent with the model predictions. We present a few of the aforementioned morphological features in Figure 8, overlaid on an image of Didymos and on the roughness map. A complete description of the various geological units is available in O. S. Barnouin et al. (2023), and a detailed study of boulders moving down putative avalanche runs can be found in J. Bigot et al. (2023). Here we emphasize that the roughness analysis provides additional insight that can help refine the geological interpretation.

Mobilized material close to the equator may leave the surface and be put in orbit, depending on the actual asteroid mass and equatorial extents (N. Trógolo et al. 2023). The overlap between these mass-wasted areas indicates that several events took place sequentially, and it is possible that regolith mobilization will occur again on Didymos in the near future, perhaps to be detected by the upcoming Hera mission. The ejecta mass has been measured to be at least 6×10^6 kg (F. Moreno et al. 2023), potentially up to 2.2×10^7 kg (A. Graykowski et al. 2023). Some of this material may have impacted Didymos, triggering additional mass wasting.

In summary, Didymos's morphology presents large-scale patterns in its roughness distribution, which clearly identify several distinct morphological units: smooth equatorial terrains, rougher surfaces at high latitudes, and possible mass wasting from midlatitudes toward the equator. This pattern is consistent with our current understanding of evolutionary processes that may occur on the surface of rapidly spinning asteroids. If we interpret the lobate features as evidence for mass wasting, the apparent layering could indicate that such events took place sequentially at different epochs and may be related to the spin-up process that led to the current state. This interpretation is compatible with the geological study presented in O. Barnouin et al. (2019), which concludes that Didymos is a structurally weak object with a shear strength in the range 1–10 Pa from surface to interior. This implies that the surface would be extremely prone to failure from the smallest solicitation, and mass wasting is likely to have taken place, perhaps still occurring at the present day.

Dimorphos, on the other hand, presents a much more homogeneous surface, on average rougher than Didymos. We note that we can use the roughness distribution to which separates decimeter-scale and larger boulders from the

finer regolith substrate. The roughness analysis finds no concentrated regions of dust on the surface of Dimorphos, which is confirmed by high-resolution images (O. S. Barnouin et al. 2023; R. T. Daly et al. 2023). Note that this does not mean that Dimorphos does not host dust at all (see discussion in B. J. Buratti et al. 2024), but rather that small particles are not present on the surface in large deposits. Telescopic observations, which are usually sensitive to micron-level particles, captured the ejecta plume consisting of such small particles. It is hard to consider that the DART impact generated all such dust particles because highly effective fragmentation only occurs at the impact site, meaning that the large amount of dust observed by telescopic campaigns may have existed before the impact, possibly stored in subsurface regions.

The lack of dusty regions on the surface of Dimorphos, though, suggests that the binary pair was formed relatively recently, within a timescale shorter than what is needed to create new dust from boulder erosion by meteoroid impact or thermal fatigue (0.1 Myr; A. Lucchetti et al. 2023). That is compatible with cratering studies, which indicate that the surface age of Dimorphos is significantly younger than that of Didymos, in the range 0.09–11 Myr (O. S. Barnouin et al. 2023). We also note that a detailed analysis of the morphology of Dimorphos boulders shows that they are primarily fragments of a catastrophic disruption and do not display evidence for significant subsequent erosion (C. Q. Robin et al. 2024). Whether this disruption resulted from YORP spin-up or from collisions cannot be determined by our analysis alone. However, dynamical studies (A. Campo Bagatin et al. 2023) strongly suggest that collisions have been the dominant factor driving surface evolution.

As Didymos's equatorial regions appear much smoother than Dimorphos when observed at the same scale, we suggest that these areas are likely to be covered in material finer than what we detected on Dimorphos at the highest resolution (a few centimeters).

In conclusion, several lines of evidence combine to build a picture of how the Didymos binary system came to be: the rough surface of Dimorphos, the smooth areas lacking boulders on Didymos's equatorial regions, and the relative age difference between the two bodies may be indicative of a formation process by which Dimorphos is preferentially formed from material that was shed from the primary asteroid.

The methods presented in this paper provide a novel way to assess the surface roughness of an airless body, from texture alone, or from a shape model. In both cases, our approach strives to obtain a rapid evaluation of the surface properties while minimizing the number of free parameters. We find that the RFT, based on measuring the EOI in images, is particularly robust and low in resources. This makes it a good candidate for embedded software that could support autonomous navigation, for instance, with future asteroid missions or a lunar lander. We are currently implementing the technique in the data analysis pipeline for ESA's Hera mission, which is scheduled to launch in 2024 and will fully characterize asteroids Didymos and Dimorphos at high resolution in 2026.

Acknowledgments

This work was supported by the DART mission, NASA contract No. 80MSFC20D0004. It has also received funding from the European Union's Horizon 2020 research and innovation program under grant agreement No. 870377 (project NEO-MAPP) and the Centre National d'Etudes Spatiales (CNES). A.L. and M.P. acknowledge financial support from Agenzia Spaziale Italiana (ASI-INAF contract No. 2019-31-HH.0 and No. 2022-8-HH.0). A.C.-B. acknowledges funding by EC H2020-SPACE-718 2018-2020/H2020-SPACE-2019 and by MICINN (Spain) PGC2021, PID2021-125883NB-C21. J.M.T.-R. acknowledges financial support from the project PID2021-128062NB-I00453 funded by MCIN/AEI/10.13039/501100011033. T.K. is supported by Academy of Finland project 335595 and by institutional support RVO 67985831 of the Institute of Geology of the Czech Academy of Sciences.

Appendix A
Data Availability

All data used in this article are publicly available on NASA's Planetary Data System archive (https://pds-smallbodies.astro.umd.edu/), including images, associated documentation, and advanced products like the asteroid shape models. Table A1 lists the shape models used in this study, and reference publications in which the models are described. All files are publicly available

Reference images used in this study: 67P, N20140903T034422640ID20F22; Itokawa, st_2474846738_v; Bennu, 20181113T045713S212_pol_L1pan; Didymos, dart_0401929888_05627_01_iof; Dimorphos, dart_0401930040_12262_01_iof.

Table A1
Reference Shape Models (Latest Version Available at the Time of This Study)

Object	Shape Model Version	Reference
67P	cg-dlr_spg-shap7-v1.0	F. Preusker et al. (2017)
Itokawa	HAY-A-AMICA-5-ITOKAWASHAPE-V1.0;	R. Gaskell et al. (2021)
Bennu	bennu_g_00400mm_alt_ptm_0000n00000_v021	OSIRIS-REx Altimetry WG (2021)
Didymos	data_derived_didymos_model_v003::1.0	T. Daly et al. (2023)
Dimorphos	data_derived_dimorphos_model_v004::1.0	T. Daly et al. (2023)

Appendix B
Code Availability

The image analysis performed in this paper is based on publicly available Python libraries; links to the relevant repositories have been provided in the text. The shape model analysis is based on custom C code added to the free scientific software shapeViewer (J. B. Vincent 2018), available at https://www.comet-toolbox.com/shapeViewer.html. Because the code relies on other parts of the software to load the shape model and display the results on the screen, it is difficult to isolate from the large codebase of shapeViewer. Instead, we opted for providing the detailed algorithm in Section 2.2 rather than the actual implementation. The compiled software is freely available to verify our results. Code can be made available on request.

ORCID iDs

Jean-Baptiste Vincent https://orcid.org/0000-0001-6575-3079
Erik Asphaug https://orcid.org/0000-0003-1002-2038
Olivier Barnouin https://orcid.org/0000-0002-3578-7750
Paula G. Benavidez https://orcid.org/0000-0001-6569-0223
Tomáš Kohout https://orcid.org/0000-0003-4458-3650
Sabina D. Raducan https://orcid.org/0000-0002-7478-0148

References

Barnouin, O., Daly, M., Palmer, E., et al. 2019, NatGe, 12, 247
Barnouin, O. S., Ballouz, R. L., Marchi, S., et al. 2023, NatCo, 15, 6202
Bigot, J., Lombardo, P., Murdoch, N., et al. 2023, NatCo, 15, 6204
Buratti, B. J., Pittichová, J., Mishra, I., et al. 2024, PSJ, 5, 83
Campo Bagatin, A., Dell'Oro, A., Parro, L. M., et al. 2023, NatCo, 15, 3714
Daly, M. G., Barnouin, O. S., Seabrook, J. A., et al. 2020, SciA, 6, eabd3649
Daly, R. T., Ernst, C. M., Barnouin, O. S., et al. 2023, Natur, 616, 443
Daly, T., Barnouin, O., Ernst, C., et al. 2023, DART Shapemodel Archive Bundle, NASA Planetary Data System, urn:nasa:pds:dart_shapemodel::1.0, doi:10.26007/96fn-p578
Egorov, M., Boldrin, L., & Tancredi, G. 2017, Asteroids, Comets, Meteors Conf., http://acm2017.uy/abstracts/Poster1.e.15.pdf
Ernst, C., Daly, T., Barnouin, O., & Espiritu, R. 2023, Draco Calibrated Data Collection for the Didymos Reconnaissance and Asteroid Camera for OpNav (DRACO) instrument v2.0, NASA Planetary Data System, urn:nasa:pds:dart:data_dracocal::2.0, doi:10.26007/trxj-vt70
Fletcher, Z. J., Ryan, K. J., Ernst, C. M., et al. 2022, Proc. SPIE, 12180, 121800E
Fujiwara, A., Kawaguchi, J., Yeomans, D. K., et al. 2006, Sci, 312, 1330
Garland, M., & Heckbert, P. S. 1997, in SIGGRAPH '97: Proc. 24th Annual Conf. on Computer Graphics and Interactive Techniques (New York: ACM), 209
Garvin, J. B., Sakimoto, S. E., Frawley, J. J., & Schnetzler, C. 2000, Icar, 144, 329
Gaskell, R., Saito, J., Ishiguro, M., et al. 2021, Gaskell Itokawa Shape Model V1.1, NASA Planetary Data System, urn:nasa:pds:gaskell.ast-itokawa.shape-model::1.1, doi:10.26033/3B2J-YY57
Gonzalez, R., & Woods, E. 2008, Digital Image Processing (New York: Pearson Education Ltd.)
Gowman, G., Cotto-Figueroa, D., & Ryan, A. 2023, PSJ, 4, 187
Graykowski, A., Lambert, R. A., Marchis, F., et al. 2023, Natur, 616, 461
Hanuš, J., Delbo', M., Durech, J., & Alí-Lagoa, V. 2018, Icar, 309, 297
Hapke, B. 1984, Icar, 59, 41
Hasselmann, P. H., Fornasier, S., Barucci, M. A., et al. 2021, Icar, 357, 114106
Heim, L.-O., Blum, J., Preuss, M., & Butt, H.-J. 1999, PhRvL, 83, 3328
Herrmann, C., & Vincent, J.-B. 2024, EPSC, 17, EPSC2024–418
Hirabayashi, M., Ferrari, F., Jutzi, M., et al. 2022, PSJ, 3, 140
Hirabayashi, M., Nakano, R., Tatsumi, E., et al. 2020, Icar, 352, 113946
Hirabayashi, M., & Scheeres, D. J. 2019, Icar, 317, 354
Jaumann, R., Schmitz, N., Ho, T.-M., et al. 2019, Sci, 365, 817
Jawin, E. R., McCoy, T. J., Walsh, K. J., et al. 2022, Icar, 381, 114992
Kreslavsky, M. A., Head, J. W., Neumann, G. A., et al. 2013, Icar, 226, 52
Li, B., Ling, Z., Zhang, J., et al. 2015, P&SS, 117, 303
Lucchetti, A., Cambioni, S., Nakano, R., et al. 2023, NatCo, 15, 6206
Marshal, R. M., Rüsch, O., Wöhler, C., Wohlfarth, K., & Velichko, S. 2023, Icar, 394, 115419
Marshall, D., Groussin, O., Vincent, J. B., et al. 2018, A&A, 616, A122
Michel, P., Küppers, M., Bagatin, A. C., et al. 2022, PSJ, 3, 160
Moreno, F., Bagatin, A. C., Tancredi, G., et al. 2023, PSJ, 4, 138
Naidu, S. P., Benner, L. A. M., Brozovic, M., et al. 2020, Icar, 348, 113777
OSIRIS-REx Altimetry WG 2021, g_00400mm_alt_ptm_0000n00000_v021, NASA Planetary Data System, urn:nasa:pds:context:target:asteroid.101955_bennu
Otto, K. A., Matz, K.-D., Schröder, S. E., et al. 2020, MNRAS, 500, 3178
Pajola, M., Tusberti, F., Lucchetti, A., et al. 2023, NatCo, 15, 6205
Palmer, E. E., Daly, R. T., Ernst, C. M., et al. 2022, AGUFM, P55F–1627
Preusker, F., Scholten, F., Matz, K. D., et al. 2017, A&A, 607, L1
Robin, C. Q., Duchene, A., Murdoch, N., et al. 2024, NatCo, 15, 6203
Sánchez, P., & Scheeres, D. J. 2014, M&PS, 49, 788
Scheeres, D., Hartzell, C., Sánchez, P., & Swift, M. 2010, Icar, 210, 968
Shannon, C. E. 1948, BSTJ, 27, 379
Shepard, M. K., Campbell, B. A., Bulmer, M. H., et al. 2001, JGR, 106, 32777
Sugita, S., Honda, R., Morota, T., et al. 2019, Sci, 364, eaaw0422
Susorney, H. C., & Barnouin, O. S. 2018, Icar, 314, 299
Susorney, H. C. M., Barnouin, O. S., Ernst, C. M., & Byrne, P. K. 2017, JGRE, 122, 1372
Susorney, H. C. M., Johnson, C. L., Barnouin, O. S., et al. 2019, Icar, 325, 141
Thomas, C. A., Naidu, S. P., Scheirich, P., et al. 2023, Natur, 616, 448
Thomas, N., Barbieri, C., Keller, H. U., et al. 2012, P&SS, 66, 96
Thomas, N., El Maarry, M. R., Theologou, P., et al. 2018, P&SS, 164, 19
Thomas, P. C., Joseph, J., Carcich, B., et al. 2002, Icar, 155, 18
Trógolo, N., Campo Bagatin, A., Moreno, F., & Benavidez, P. G. 2023, Icar, 397, 115521
Varnes, D. J. 1976, GeoM, 113, 300
Vincent, J. B., Hviid, S. F., Mottola, S., et al. 2017, MNRAS, 469, S329
Vincent, J. B. 2018, LPSC, 49, 1281
Vincent, J.-B., Kruk, S., Fanara, L., Birch, S., & Jindal, A. 2021, EPSC, 15, EPSC2021–525
Walsh, K. J., Richardson, D. C., & Michel, P. 2012, Icar, 220, 514
Watanabe, S., Hirabayashi, M., Hirata, N., et al. 2019, Sci, 364, 268
Zhang, Y., Michel, P., Richardson, D. C., et al. 2021, Icar, 362, 114433